

# Thermoacoustic tomography with correction for acoustic speed variations

Xing Jin<sup>1</sup> and Lihong V Wang<sup>2</sup>

<sup>1</sup> Department of Biomedical Engineering, Texas A&M University, College Station, Texas 77843-3120, USA

<sup>2</sup> Department of Biomedical Engineering, Washington University in St Louis, St Louis, MO 63130-4899, USA

E-mail: [lhwang@biomed.wustl.edu](mailto:lhwang@biomed.wustl.edu)

Received 5 September 2006, in final form 19 October 2006

Published 28 November 2006

Online at [stacks.iop.org/PMB/51/6437](http://stacks.iop.org/PMB/51/6437)

## Abstract

Thermoacoustic tomography (TAT) is a technique that measures microwave-induced thermoacoustic waves at the boundary of biological tissue and generates images of internal microwave absorption distributions from the measurements. Existing reconstruction algorithms for TAT are based on the assumption that the acoustic properties in the tissue are homogeneous. Biological tissue, however, has heterogeneous acoustic properties, which lead to distortion and blurring of small buried objects in the reconstructed images. In this paper we develop a correction method based on ultrasonic transmission tomography (UTT) to improve the image quality of TAT. Numerical simulations and phantom experiments verify the effectiveness of this correction method.

(Some figures in this article are in colour only in the electronic version)

## 1. Introduction

Thermoacoustic tomography (TAT) has been developed to overcome the limitations of both conventional ultrasound and microwave imaging. In TAT, pulsed microwave energy is delivered into biological tissue through a waveguide. The electromagnetic energy absorbed by the biological tissue induces an ultrasonic wave via thermoelastic expansion, which then propagates in the tissue. The ultrasonic wave is detected by an ultrasonic transducer that is scanned around the object to reconstruct the microwave energy deposition in the tissue. The resolution of TAT is determined by the induced ultrasonic wave. The high contrast of TAT is due to differences in the microwave absorption coefficients of different biological tissues. The microwave absorption coefficients of tissues are determined by their dielectric properties. It has been reported that tumour and normal tissue differ significantly in their dielectric properties (Chaudhary *et al* 1984). Therefore, TAT has the potential for applications

in tumour detection and treatment monitoring (Kruger *et al* 2000, 2002, Ku *et al* 2005, Jin *et al* 2005, Xu and Wang 2006). One of the potential applications for TAT is early breast cancer detection. The American Cancer Society reports that breast cancer is the second overall leading cause of death among women in the United States. The mortality rate from breast cancer has declined in recent years due to progress in both early detection and more effective treatments. Better detection techniques, however, are still needed. X-ray mammography and ultrasonography are most commonly used clinical tools for breast cancer screening and detection. However, mammography uses ionizing radiation and has difficulty imaging premenopausal breasts, which are radiographically dense. Ultrasonography is operator dependent. It suffers from not being able to provide quantitative information, and thus is used mostly as a complementary tool to mammography. Ultrasound computed tomography is a new imaging modality that shows higher resolution and better contrast than ultrasonography. Ultrasound specificity in breast cancer detection, however, is limited by the overlapping acoustic characteristics of benign and malignant solid lesions. In addition, ultrasound imaging may also miss tiny nonpalpable breast tumours, which have low acoustic contrast. Because the dielectric properties of normal and malignant tissues are found to vary appreciably over a range of frequencies, microwave-induced TAT holds promise for the early detection of tumours.

Existing reconstruction algorithms for TAT is based on the assumption of homogeneous acoustic speed in biological tissue, an approximation that is only partially valid in clinical application. From breast imaging with TAT, we have learned that different components of the breast, such as the glandular tissues, stromal tissues, cancerous tissues and other fatty tissues, have different acoustic properties (Duck 1990). The variations between their acoustic speeds can be as great as 10%. The acoustic speed in subcutaneous fat is between  $1400 \text{ m s}^{-1}$  and  $1450 \text{ m s}^{-1}$ , whereas the acoustic speed in normal parenchyma and stromal tissue is between  $1500 \text{ m s}^{-1}$  and  $1560 \text{ m s}^{-1}$ .

Acoustic speed variations have two effects on TAT images based on the homogeneous-speed assumption. The first effect is the displacement of thermoacoustic signals radially, i.e. along the assumed linear radiating propagation paths of a thermoacoustic signal, due to an incorrect acoustic speed being assumed in calculating the positions of targets along the path. The second effect is the displacement of thermoacoustic signals tangentially due to the ultrasonic refraction away from the assumed straight path. In existing reconstruction algorithms, the recorded acoustic signals from a given viewing angle are backprojected to the imaging region without position correction. Therefore, the backprojected signals from a given detection position are misplaced in the reconstructed image and subsequently added imprecisely to the backprojected signals obtained from other detection positions. This causes both blurring and displacement in the reconstructed image and reduces the contrast. Consequently, the ability of TAT to detect small tumours is compromised.

A numerical study showed that the effects of acoustic heterogeneities on TAT can be reduced by using an acoustic speed distribution (Xu and Wang 2003), which is measured independently of TAT. To this end, we use ultrasonic transmission tomography (UTT) to quantitatively measure the acoustic speed distribution in the tissue. UTT is implemented by time-of-flight measurements (Kim *et al* 1984, Jago and Whittingham 1991, Clover and Sharp 1977, Chenevert *et al* 1984), and it is compatible with our TAT system. Since UTT reveals mechanical contrast, the image quality of UTT alone is insufficient for early-stage tumour detection. The deterioration of the image quality due to ultrasonic attenuation and refraction is less significant in TAT than in UTT, because in TAT the ultrasonic wave propagates one way only and the central frequency of the generated thermoacoustic waves is lower (around 1 MHz).

In this paper, we analyse the effects of acoustic speed variations on TAT imaging and then propose a compensation method based on UTT to correct for these effects. We show that the acoustic speed distributions obtained from UTT can be used to improve the image quality of TAT in weakly refractive tissue. Numerical simulations and phantom experiments are presented to verify the effectiveness of the proposed method.

## 2. Theoretical basics and methods

### 2.1. Measurement of the speed-of-sound distribution

To correct for the effects of acoustic speed heterogeneities, we need to measure the acoustic speed distribution. In this preliminary research, the measurement of two-dimensional (2D) acoustic speed distributions is achieved by UTT. The relationship between the speed-of-sound image and measurements obtained for UTT will be explained.

In UTT, the acoustic speed in biological tissue can be calculated from the arrival times of ultrasonic waves. The total travel time of an acoustic signal is given by the integral of the inverse of the acoustic speed in the tissue along the ray path:

$$T = \int_{l(\mathbf{r})} \frac{1}{c(\mathbf{r})} dl \quad (1)$$

where  $c(\mathbf{r})$  is the acoustic speed in the tissue and  $l(\mathbf{r})$  is the ray path. The total travel time  $T$  can be measured from the recorded ultrasonic signals. The time-of-flight measurement for a specific projection line is computed by a cross-correlation operation between the signals from the ultrasonic transmitter and the signals from the ultrasonic receiver. The location of the maximum of the cross-correlation represents the time-of-flight of the ultrasonic wave in the tissue. Since  $l(\mathbf{r})$  depends on  $c(\mathbf{r})$ , the relationship between  $T$  and  $1/c(\mathbf{r})$  is nonlinear in general. Below, we linearize this problem.

The travel-time perturbation  $\delta T$  is defined as

$$\delta T = T - T_0 \quad (2)$$

where  $T$  and  $T_0$  denote the total travel times of the ultrasonic pulse traversing through the medium with, and without, speed heterogeneities present, respectively. A homogenous reference medium is used to measure  $T_0$ . The travel times are considered stationary here (Snieder and Aldridge 1995, Berryman 1989). For weakly refractive tissues, we linearize  $l(\mathbf{r})$  to the reference ray in the homogenous reference medium,  $l(\mathbf{r}_0)$ , which is independent of  $c(\mathbf{r})$ . As a result, we have

$$\delta T = \int_{l(\mathbf{r}_0)} \left( \frac{1}{c(\mathbf{r})} - \frac{1}{c_0} \right) dl \quad (3)$$

where  $c_0$  denotes the acoustic speed of the homogenous reference medium. The integration is now taken over  $l(\mathbf{r}_0)$ . Since  $l(\mathbf{r}_0)$  is assumed to be straight, equation (3) represents a linear relationship between  $\delta T$  and the difference in the inverse of the acoustic speed and is a form of the Radon transform. This equation sets up the relationship between the acoustic speed distribution in the tissue and the measurements obtained from UTT. Of course, equation (3) is valid only for weakly refractive tissue. If strong bending of ultrasonic rays occurs as they cross strongly refractive tissue, equation (3) is no longer valid.

To implement UTT based on equation (3), we divide the two-dimensional imaging area into cells and assume that  $c(\mathbf{r})$  remains constant in each cell. For viewing angle  $i$ , we let  $l_{ij}$  be the length of the path that the ultrasound pulse transverses through cell  $j$ . The discretized

form of equation (3) is then written as

$$\delta T_i = \sum_j l_{ij} \left( \frac{1}{c_j} - \frac{1}{c_0} \right) \quad (4)$$

where  $c_j$  is the acoustic speed in cell  $j$ . The nonlinear problem in equation (1) has been simplified to a system of linear equations. To solve equation (4) for the acoustic speed distribution in the tissue, we simply perform a linear inversion using a filtered back-projection method (Kak and Slaney 1988).

## 2.2. Effects of acoustic speed variations on TAT and the correction method

The propagation of thermoacoustic waves is governed by the following partial differential equation (Diebold *et al* 1991, Xu and Wang 2002):

$$\nabla^2 p(\mathbf{r}, t) - \frac{1}{c^2(\mathbf{r})} \frac{\partial^2 p(\mathbf{r}, t)}{\partial t^2} = -\frac{\beta}{C_p} \frac{\partial H(\mathbf{r}, t)}{\partial t}. \quad (5)$$

Here,  $\beta$  is the volume thermal expansion coefficient,  $C_p$  is the specific heat,  $p(\mathbf{r}, t)$  is the measured pressure at a certain position and time,  $c(\mathbf{r})$  is the acoustic speed distribution in the tissue, and  $H(\mathbf{r}, t)$  is the thermal deposition function at a certain position and time. The thermal deposition function can be written as the product of a spatial energy deposition function and a microwave pulse function  $H(\mathbf{r}, t) = \varphi(\mathbf{r}) \cdot I(t)$ , where  $\varphi(\mathbf{r})$  denotes the energy deposition in the tissue, and  $I(t)$  denotes the microwave pulse function. Equation (5) is derived by neglecting tissue blood perfusion and thermal diffusion. Because the microwave pulse duration is at sub- $\mu$ s level and the heating is relatively homogeneous within the same type of tissue, the heat transferred by blood perfusion is much less than the electromagnetic energy absorbed by the tissue within the pulse duration. Thus we neglect the effects of blood perfusion. Thermal diffusion length is proportional to the square root of the multiplication of the thermal diffusivity of the tissue sample and the microwave pulse duration (Tam 1986). Thermal diffusivity for most soft biological tissues is around  $1.4 \times 10^{-3} \text{ cm}^2 \text{ s}^{-1}$  (Duck 1990). The microwave pulse duration was set to be  $0.5 \mu\text{s}$  in our experiment. The thermal diffusion length is thus estimated to be at the  $\mu\text{m}$  level, which is much less than the  $0.5 \text{ mm}$  system resolution of TAT (Xu and Wang 2002) and  $\text{cm}$  scale penetration depth of microwave in the tissue. Therefore we can neglect the thermal diffusion in our analysis.

By assuming  $I(t) = \delta(t)$  (Dirac delta function), and performing a Fourier transform with respect to  $t$  on both sides of the equation, we obtain

$$\left( \nabla^2 + \frac{\omega^2}{c^2(\mathbf{r})} \right) \tilde{p}(\mathbf{r}, \omega) = -i\omega \frac{\beta}{C_p} \cdot \varphi(\mathbf{r}) \quad (6)$$

where  $\omega$  is the angular frequency,  $\tilde{p}(\mathbf{r}, \omega)$  is the Fourier transform of  $p(\mathbf{r}, t)$  with respect to  $t$ , and  $\tilde{p}(\mathbf{r}, \omega) = \int_{-\infty}^{\infty} p(\mathbf{r}, t) \cdot \exp(-i\omega t) dt$ .

In an acoustically homogeneous medium, we have  $c(\mathbf{r}) = c$  (constant). For spherical detection geometry,  $p(\mathbf{r}, t)$  can be solved by using Green's function approach:

$$p(\mathbf{r}, t) = \frac{c\beta}{4\pi C_p} \frac{\partial}{\partial t} \oint_{t=|\mathbf{r}-\mathbf{r}'|/c} \frac{\varphi(\mathbf{r}')}{|\mathbf{r}-\mathbf{r}'|} d\mathbf{r}'. \quad (7)$$

The integration, representing the forward problem, is performed on a spherical surface. The associated inverse problem has been investigated by many researchers. The back-projection solutions for different detection geometries can be found in Xu *et al* (2003). In our experiment, a circularly scanning detection geometry is used. An approximate back-projection solution

for this 2D detection geometry in the time domain can be written as (Xu *et al* 2004)

$$\varphi(\mathbf{r}') \approx \frac{C_P}{c^2 \beta} \int_{d\theta} \left. \frac{\partial p(\mathbf{r}, t)}{\partial t} \right|_{t=|\mathbf{r}-\mathbf{r}'|/c}. \quad (8)$$

The integration is performed over all of the scanning angles. In real situations, the effect of the microwave pulse duration and the impulse function of the receiving transducer may be incorporated (Xu and Wang 2002).

In an acoustically inhomogeneous medium, numerical methods based on linear approximations are used to provide the inverse solution for TAT. For weakly refractive tissue, the time profile of the thermoacoustic wave is dominated by the first-order acoustic speed component, and the distortion of the time profile of the thermoacoustic wave is mainly determined by the first-order perturbation. By contrast, higher-order acoustic speed components determine the spatial distribution of the ultrasonic waves. Here, we neglect the high-order acoustic speed components and only implement axial acoustic corrections. The received thermoacoustic wave can, therefore, be approximately modelled by the following integral over a perturbed sphere:

$$p(\mathbf{r}, t) \approx \frac{c\beta}{4\pi C_p} \frac{\partial}{\partial t} \oint_{\tilde{S}} \frac{\varphi(\mathbf{r}'')}{|\mathbf{r} - \mathbf{r}''|} d\mathbf{r}'' \quad (9)$$

where  $\tilde{S}$  is a curved surface on which every point source has the same time-of-flight to the receiver, and  $\mathbf{r}''$  denotes the position of a point source on  $\tilde{S}$ .

The problem then becomes finding  $\varphi(\mathbf{r})$  by minimizing  $\|L(\varphi(\mathbf{r})) - \hat{p}(\mathbf{r}, t)\|$ . Here,  $\hat{p}(\mathbf{r}, t)$  is the measured pressure (projection data),  $L$  is a linear operator that consists of a summation on  $\tilde{S}$  followed by a time differentiation in the time-domain:

$$L_\varphi(\mathbf{r}, t) := \eta_0 \cdot \frac{\partial}{\partial t} \oint_{\tilde{S}} \frac{\varphi(\mathbf{r}'')}{|\mathbf{r} - \mathbf{r}''|} d\mathbf{r}'' \quad (10)$$

where  $\eta_0$  is a constant. In 2D, the integration is performed along a perturbed circle. Here, we use LSQR to solve the optimization problem, where LSQR is a least-squares method that uses an iterative approach to generate a sequence of approximations so that the residual norm decreases monotonically (Paige and Saunders 1982). This method depends on the initial estimate of the energy deposition, which is obtained from the constant-speed model.

LSQR is selected for its robustness. The algorithm is summarized as follows:

- (1) The acoustic speed distribution is calculated from the time-of-flight measurements obtained by UTT through a filtered back-projection method. The acoustic speeds at specific locations are obtained using bilinear interpolation.
- (2) An initial estimate of the energy deposition  $\varphi(\mathbf{r})$  is made from the measurements of projection data  $\hat{p}(\mathbf{r}, t)$  by using equation (8).
- (3) An iterative least-squares method based on LSQR is used to solve  $\|L(\varphi(\mathbf{r})) - \hat{p}(\mathbf{r}, t)\|$ . The iteration stops when either the maximum number of iterations has been reached or the corresponding criterion for the convergence is satisfied.

### 3. Experimental system

An experimental system was constructed based on our current TAT set-up to obtain both speed-of-sound and TAT images. The combined TAT/UTT set-up is schematically shown in figure 1(a), and the scanning geometry is shown in figure 1(b). The scanning system consisted of two single-element unfocused 2.25 MHz ultrasonic transducers (Panametrics Inc., V323) that were approximately 6 mm in diameter with a 6 dB bandwidth of approximately 65%.

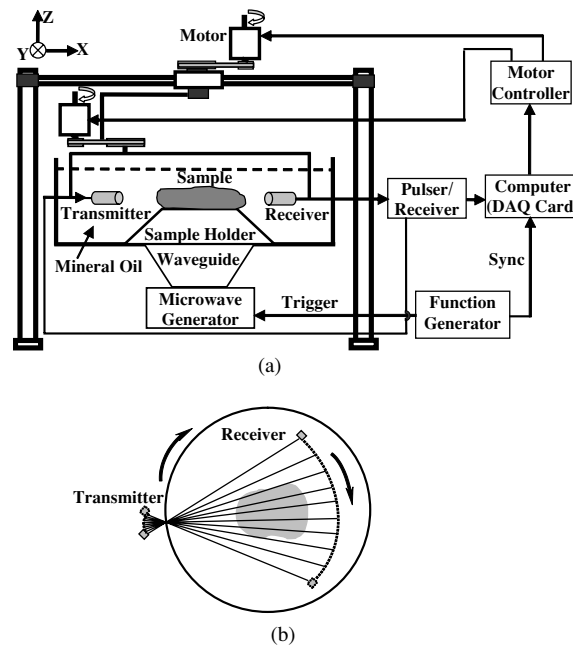


**Figure 1.** Experimental set-up and the scanning geometry: (a) experimental set-up for the combined TAT/UTT imaging system and (b) schematic of the scanning geometry in top view. In UTT, the transmitter sent pulsed ultrasonic signals, and the receiver on the opposite side of the transmitter received the ultrasonic pulses. In TAT, the transmitter used in UTT was used as the receiver, which circularly scanned the tissue sample.

The to-be-measured samples were immersed in mineral oil, which was used as the acoustic coupling medium in the experiments.

For UTT, two unfocused ultrasonic transducers were required. One was used to transmit the ultrasonic pulses and the other, on the opposite side of the transmitter, was used to receive the pulses. Image reconstruction required fan-beam scanning as well as circular scanning of the two transducers. Both the transmitting and receiving transducers were mounted on a mechanical arm that was driven by two stepping motors to scan the tissue sample submerged in mineral oil. The mechanical arm first scanned in a fan-beam fashion to cover the target region of a  $67.5^\circ$  fan-beam angle at each projection angle in 120 steps by a stepping motor. Then, the two ultrasonic transducers at the positions along the centre axis of the fan beam were rotated circularly in the imaging plane with a step size of  $2.25^\circ$  by a second stepping motor. A pulser-receiver (PR 5072, Panametrics Inc.) was used to transmit and to receive the ultrasound pulses. The data were collected by using a PC-based data acquisition card (CS14200, Gage Inc.). The time-of-flight measurements of the transmitted pulses were made using the cross-correlation method. An acoustic speed image was then reconstructed using a filtered backprojection method on a  $200 \times 200$  grid. The speed-of-sound images were subsequently used to correct distortion and blurring in the TAT images of the same target.

For TAT, because the thermoacoustic waves were induced by electromagnetic radiation, we did not need an ultrasonic transducer as a transmitter. Either one of the two transducers could be used as the detector for the generated thermoacoustic signals. The central frequency of the microwave pulse was 3 GHz, the peak power of microwave source was around 10 KW, the pulse width was  $0.5 \mu\text{s}$ , and the pulse repetition rate is 20 Hz. In the experiment,

only part of the microwave energy was coupled out of the waveguide. The estimated peak power that was delivered to the tissue was about 2 kW. The received thermoacoustic signals were amplified by the ultrasonic amplifier and then sampled by the data acquisition board. At each scan position, 150 measurements were averaged. Current research shows that thermal changes account for most of the bioeffects of absorbed electromagnetic energy on human subjects (Adair and Petersen 2002, Gajek *et al* 2003). Acceptable electromagnetic exposure for human beings has been evaluated by the specific absorption rate (SAR), which is defined as the time-averaged rate of energy absorbed per unit volume divided by the mass of the volume ( $\text{W kg}^{-1}$ ) inside an absorber. The ANSI-IEEE Criterion for the average SAR in the whole body is under  $0.4 \text{ W kg}^{-1}$ . The estimated SAR based on the above microwave source conforms to the safety requirements.

The UTT data were collected first, and then the TAT measurements were recorded. We performed phantom experiments on the same tissue sample using both UTT and TAT. The TAT image without acoustic speed compensation was reconstructed by using a modified back-projection method. The TAT image with acoustic speed compensation was reconstructed by using the method discussed in the previous section.

#### 4. Results and discussion

We first used numerical simulations to demonstrate the distortion and blurring of small absorbers caused by acoustic speed variations in TAT images. Then, we used the method discussed in the previous section to compensate for the distortion and blurring in the simulated data. The compensation method was further verified by using a phantom experiment. In the following discussion, we assume refraction effects are relatively weak in the tissue.

Usually we can optimize TAT images by simply adjusting the average acoustic speed in the tissue while assuming that the medium is acoustically homogeneous. The image quality of TAT, however, is significantly limited when the acoustic speed variations are no longer negligible compared with the average acoustic speed. Figure 3 shows a numerical example of the distortion and blurring brought about by acoustic speed heterogeneities. A strong small microwave absorber was surrounded by acoustically heterogeneous tissue. The object function for TAT is shown in figure 2(a), while the object (speed-of-sound) function for UTT is shown in figure 2(b). To make the simulation results closer to the real situation, in the computation we added 2% Gaussian noise in the object (speed-of-sound) function for UTT. Part of the waves generated by the small absorber passed through the acoustically heterogeneous tissue. If we assume constant acoustic speed in the tissue, the time-of-flight error deteriorates the strength of the reconstructed absorber because the back-projection registers the thermoacoustic signals at incorrect positions. To illustrate the effects more clearly, we show a close-up TAT image of the small absorber, marked by the white dotted square in figure 2(a). The small absorber appears as a crescent-like object in figure 2(c), which has low spatial resolution. By adjusting the average acoustic speed, we can get a sharp boundary for either the big absorber or the small absorber, but not for both. Figure 2(d) shows that the distortion has been alleviated by the proposed correction method using the speed-of-sound distribution in the same sample.

We then investigated the performance of the proposed method with a phantom experiment. The phantom sample was composed of porcine fat and muscle. One large porcine muscle was embedded in the porcine fat. Figure 3(a) shows the top view of the phantom sample. The lateral size of the phantom sample was approximately  $61 \text{ mm} \times 39 \text{ mm}$ , and the thickness of the sample was around 12 mm. The sizes of the muscle were approximately  $17 \text{ mm} \times 21 \text{ mm}$ . One small strong absorber was buried near the larger piece of muscle. The diameter of the small absorber was  $\sim 2.5 \text{ mm}$ . The absorbers were constructed from porcine muscle to take

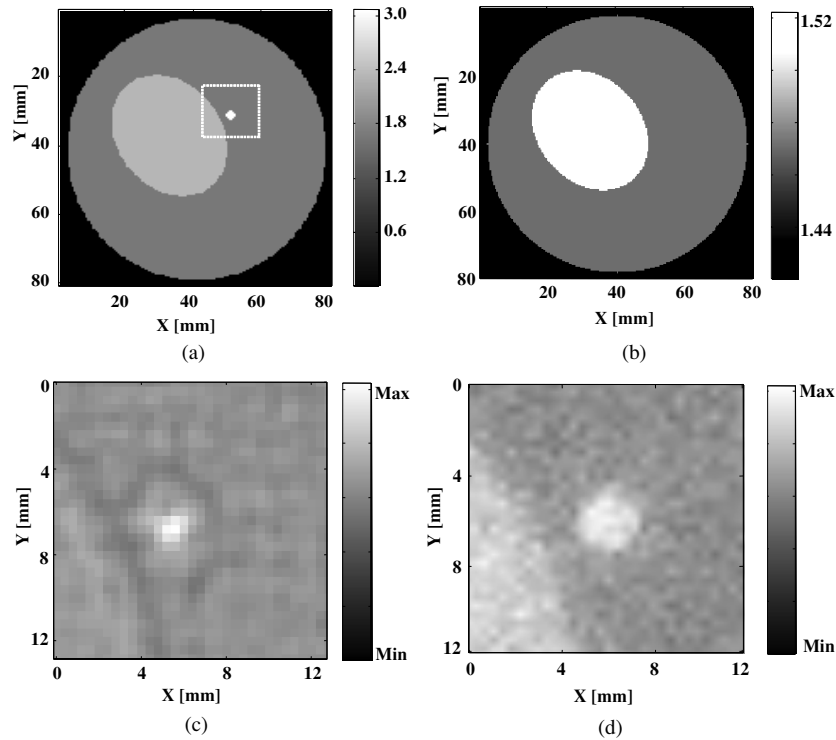


**Figure 2.** Numerical simulation: (a) object function (distribution of microwave absorption) for TAT in the simulated phantom sample and (b) object function (acoustic speed distribution) for UTT in the sample. To illustrate the blurring more clearly, we only showed the close-up TAT image of the small absorber as marked by the white dotted square in (a). (c) Close-up TAT image without correction for the acoustic speed variations and (d) close-up TAT image with correction for acoustic speed variations.

advantage of its strong absorption of microwave energy. The whole sample was immersed in mineral oil during the experiment. The phantom sample was designed to include within it relatively large acoustic speed variations. The measured acoustic speed in the porcine fat was about  $1.44 \text{ mm } \mu\text{s}^{-1}$ , and the measured acoustic speed in the porcine muscle was about  $1.54 \text{ mm } \mu\text{s}^{-1}$ . We compare the result that was acquired with the acoustic speed compensation method with the result that was acquired with the average acoustic speed adjustment method in figures 3(c) and 3(d). To better illustrate the results, we only show the close-up TAT images of the small absorber. First we reconstruct a focused TAT image by adjusting the average acoustic speed to obtain the sharpest boundary for the porcine fat and larger piece of muscle. We obtained a blurred image for the small absorber, as marked by white arrows in figure 3(c). The TAT image obtained by the acoustic speed compensation method is shown in figure 3(d). The boundary of the small absorber obtained by the proposed method is sharper than that obtained by the method without considering the acoustic heterogeneities. The blurring of the small absorber is also not as serious in figure 3(d) as that in figure 3(c).

The performance of the proposed method was further investigated by using another phantom experiment with two large porcine muscles buried in a piece of porcine fat. The top view of the phantom sample is shown in figure 4(a). The size of the whole phantom sample was approximately  $52 \text{ mm} \times 84 \text{ mm}$ , and the thickness of the sample was around

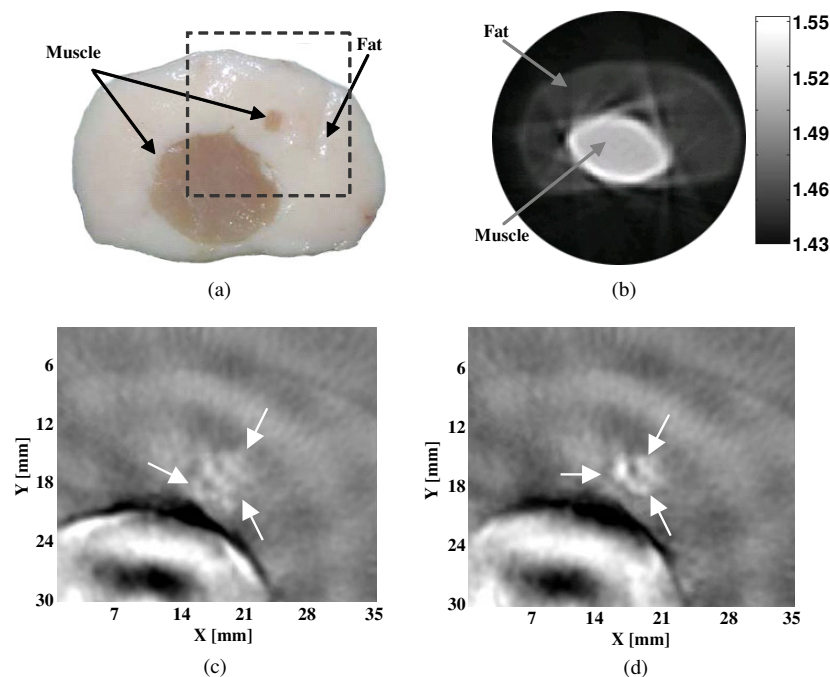


**Figure 3.** Phantom experiment: (a) photograph of the phantom sample in top view; (b) the speed-of-sound image of the phantom sample. To illustrate the blurring more clearly, we only showed the close-up TAT image of the small absorber as marked by the black dashed square in (a); (c) close-up TAT image obtained by adjusting the average acoustic speed (boundary is denoted by arrows); (d) close-up TAT image obtained by acoustic speed compensation using the acoustic speed distribution (boundary is denoted by arrows).

20 mm. The sizes of the two pieces of muscle were approximately  $14 \text{ mm} \times 25 \text{ mm}$  and  $18 \text{ mm} \times 33 \text{ mm}$ , respectively. Three small strong absorbers were embedded in the middle. The diameters of the three absorbers from top to bottom were around 2.5 mm. The acoustic speed in the porcine fat was measured to be approximately  $1.43 \text{ mm } \mu\text{s}^{-1}$ , and the acoustic speed in the porcine muscle was measured to be approximately  $1.52 \text{ mm } \mu\text{s}^{-1}$ . The acoustic speed difference between the porcine fat and porcine muscle was around 10%. Figure 4(b) shows the reconstructed speed-of-sound image, which fails to show the three small absorbers. Therefore, UTT can image large acoustic speed heterogeneity with good accuracy, but its ability to image smaller acoustic speed heterogeneity is limited. Figures 4(c) and (d) show the TAT images of the small absorbers obtained by adjusting the average acoustic speed and by acoustic-speed compensation, respectively. The three small absorbers are marked by white arrows. As can be seen, the centre of the scanning geometry has the highest resolution, whereas the outer regions have lower resolutions. Both the size and the intensity of the small absorbers are improved by the proposed acoustic speed compensation method. The improvement of the image quality is further illustrated in figures 4(e) and (f) in line plots across two of the small absorbers in the reconstructed TAT images (shown by grey arrows) in figures 4(c) and (d). The actual sizes of the absorbers are shown by the dotted circles. The size of each absorber read from the line plot based on figures 4(c) is approximately 3.0 mm in FWHM, whereas the size of each absorber read from the line plot based on figure 4(d) is around 3.5 mm in FWHM. Although the measured sizes are larger than the actual size of each absorber, the acoustic-speed

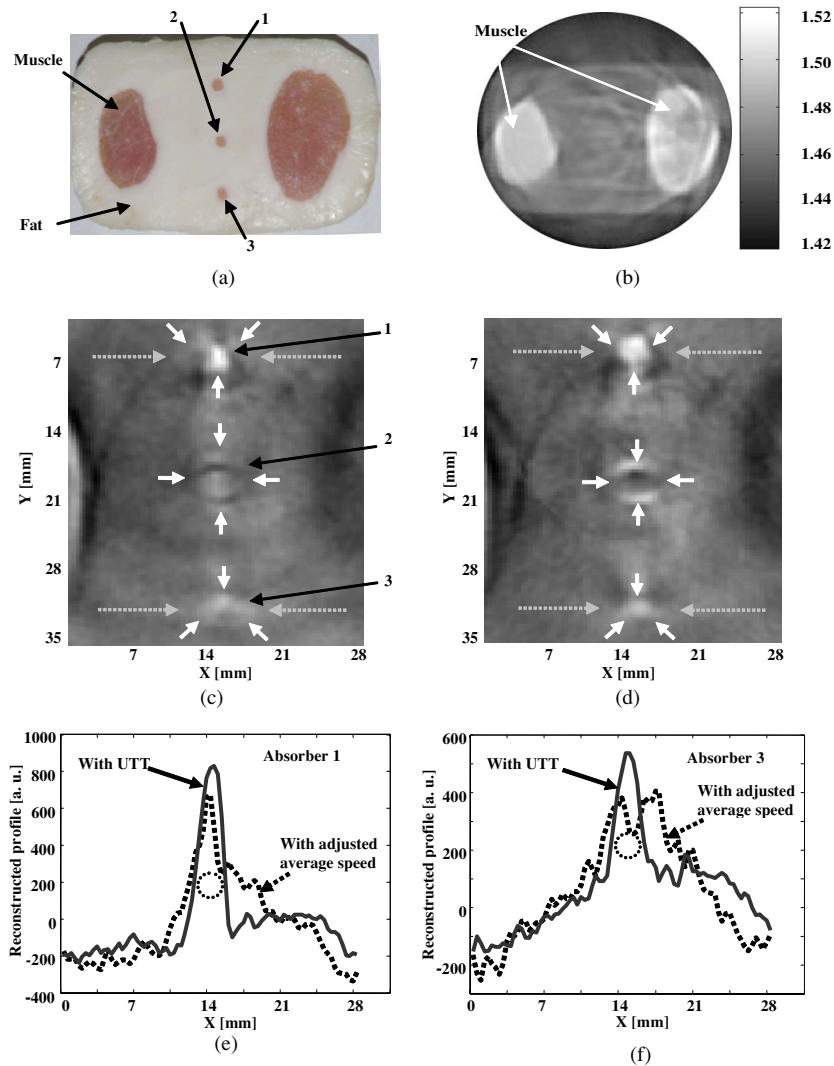


**Figure 4.** Phantom experiment: (a) photograph of the phantom sample in top view, the three absorbers were made by porcine muscle; (b) the speed-of-sound image of the phantom sample; (c) TAT image obtained by adjusting the average acoustic speed (boundaries are denoted by arrows); (d) TAT image obtained by acoustic speed compensation using the acoustic speed distribution (boundaries are denoted by arrows); (e) line plot across absorber 1 as pointed by the grey dashed arrows in (c); and (f) line plot across absorber 3 as pointed by the grey dashed arrows in (c). The actual sizes of the absorbers were shown by dotted circles in (e) and (f).

compensation method significantly increases in the ability of TAT to quantitatively define the size of the small absorbers.

The main limitation of the current experimental system is the time required to acquire the data. The data acquisition time can be greatly reduced by using a linear ultrasonic array as the receiver. If the refraction effects are small, it has been shown that the ray-tracing method can be used to improve the results of UTT (Andersen 1990, Mi and Ume 2004, Denis *et al* 1995). Also inherent in the application of the UTT algorithm is the assumption that ultrasound

pulses travel in straight lines through the target. In some applications, the refraction can be an important cause of artefacts, spatial distortion and loss of resolution. Because of refraction effects, this assumption may be increasingly invalid when acoustic speed variations are greater. For highly refractive tissue, acoustic speed compensation requires more accurate acoustic speed imaging to calculate the refracted beam paths. In such cases, we need to take special measures to improve measurements of the speed-of-sound distributions in the tissue. Mechanical inaccuracies resulting from the use of the stepped single-element transducer is another source of inaccuracies in the reconstructed acoustic speed distribution of UTT, but this error can also be alleviated by using a linear array. Compensation of TAT using UTT is also limited by other quantitative or geometrical properties of the acoustic speed images produced. For example, since the resolution of time-of-flight projections is determined by the transmitted ultrasound beam width, this represents the minimum resolution of the acoustic speed image. These limitations, however, have minimal effect on the correction of the distortion and blurring induced by relatively large acoustic speed variations in TAT.

## 5. Conclusions

We have proposed a method for using UTT to compensate for the degradation in TAT images caused by acoustic speed variations in the biological tissue. It has been shown that UTT can, within certain limitations, generate accurate and quantitative images of the acoustic speed distributions of phantoms, which results in high registration accuracy in the TAT images. It has also been shown by phantom experiments that those acoustic speed images have sufficient accuracy to compensate for the effects of acoustic speed heterogeneities in TAT images. The results obtained by this system indicate that TAT with the acoustic speed compensation is a feasible approach for obtaining higher resolution images of small tumours in acoustically heterogeneous tissues.

## Acknowledgments

We thank Geng Ku for assistance with the experimental set-up. The work was supported by the National Institutes of Health grants R01 EB000712 and R01 NS46214.

## References

- Adair E R and Petersen R C 2002 Biological effects of radio-frequency/microwave radiation *IEEE Trans. Microw. Theory Tech.* **50** 953–62
- Andersen A H 1990 Ray tracing approach to restoration and resolution enhancement in experimental ultrasound tomography *Ultrason. Imaging* **12** 268–91
- Berryman J G 1989 Fermat's principle and nonlinear travelttime tomography *Phys. Rev. Lett.* **62** 2953–56
- Chaudhary S S, Mishra R K, Swarup A and Thomas J M 1984 Dielectric properties of normal and malignant human breast tissues at radiowave and microwave frequencies *Indian J. Biochem. Biophys.* **21** 76–9
- Chenevert T L, Bylski D I, Carson P L, Meyer C R, Bland P H, Adler D D and Schmitt R M 1984 Ultrasonic computed tomography of the breast *Radiology* **152** 155–9
- Clover G H and Sharp J C 1977 Reconstruction of ultrasound propagation speed distribution in soft tissue: time-of-flight tomography *IEEE Trans. Sonics Ultrason.* **24** 229–34
- Denis F, Basset O and Gimenez G 1995 Ultrasonic transmission tomography in refracting media: reduction of refraction artifacts by curved-ray techniques *IEEE. Trans. Med. Imaging* **14** 173–88
- Diebold G J, Sun T and Khan M I 1991 Photoacoustic monopole radiation in one, two and three dimensions *Phys. Rev. Lett.* **67** 3384–7
- Duck F A 1990 *Physical Properties of Tissue: A Comprehensive Reference Book* (New York: Academic)

- Gajek P D, Andrea J A, Mason P A, Zirriax J M, Walters T J and Hurt W D 2003 *Biological Effects of Electromagnetic Field* ed P Stavroulakis (Berlin: Springer) p 116
- Jago J R and Whittingham T A 1991 Experimental studies in transmission ultrasound computed tomography *Phys. Med. Biol.* **36** 1515–27
- Jin X, Xu Y, Wang L-H, Fang Y R, Zanelli C I and Howard S M 2005 Imaging of HIFU-induced lesions in soft biological tissue using thermoacoustic tomography *Med. Phys.* **32** 5–11
- Kak A C and Slaney M 1988 *Principles of Computerized Tomographic Imaging* (Piscataway, NJ: IEEE)
- Kim J H, Park S B and Johnson S A 1984 Tomography imaging of ultrasonic reflectivity with correction for acoustic speed variations *Ultrason. Imaging* **6** 304–12
- Kruger R A, Miller K D, Reynolds H E, Kiser W L, Reinecke D R and Kruger G A 2000 Breast cancer *in vivo*: contrast enhancement with thermoacoustic CT at 434 MHz-feasibility study *Radiology* **216** 279–83
- Kruger R A, Stantz K M and Kiser W L 2002 Thermoacoustic CT of the breast *Proc. SPIE* **4682** 521–25
- Ku G, Fornage B D, Jin X, Xu M, Hunt K K and Wang L-H 2005 Thermoacoustic and photoacoustic tomography of thick biological tissues toward breast imaging *Technol. Cancer Res. Treat.* **4** 559–66
- Mi B and Ume I C 2004 Three-dimensional ray tracing laser ultrasound for weld penetration sensing *J. Acoust. Soc. Am.* **115** 1565–71
- Paige C C and Saunders M A 1982 LSQR: an algorithm for sparse linear equations and sparse least squares *ACM Trans. Math. Softw.* **8** 43–71
- Snieder R and Aldridge D F 1995 Perturbation theory for travel times *J. Acoust. Soc. Am.* **98** 1565–69
- Tam A C 1986 Applications of photoacoustic sensing techniques *Rev. Mod. Phys.* **58** 381–431
- Xu M, Xu Y and Wang L-H 2003 Time-domain reconstruction algorithms and numerical simulations for thermoacoustic tomography in various geometries *IEEE Trans. Biomed. Eng.* **50** 1086–99
- Xu M and Wang L-H 2002 Time-domain reconstruction for thermoacoustic tomography in a spherical geometry *IEEE Trans. Med. Imaging* **21** 814–22
- Xu Y, Ambartsoumian G, Kuchment P and Wang L-H 2004 Reconstructions in limited-view thermoacoustic tomography *Med. Phys.* **31** 724–33
- Xu Y and Wang L-H 2006 Rhesus monkey brain imaging through intact skull with thermoacoustic tomography *IEEE Trans. Ultrason. Ferroelectr. Freq. Control* **53** 542–8
- Xu Y and Wang L-H 2003 Effects of acoustic heterogeneity in breast thermoacoustic tomography *IEEE Trans. Ultrason., Ferroelectr. Freq. Control* **50** 1134–46